Earth Planet. Sci. Lett. 671 (2025) 119623

Contents lists available at ScienceDirect

Earth and Planetary Science Letters

journal homepage: www.elsevier.com/locate/epsl

Spatial patterns of volcanism between adjacent rift segments

Valentina Armeni [a,*], Lorenzo Mantiloni [b,c], Bodo Bookhagen [a], Eleonora Rivalta [b,d], Valerio Acocella [e], Manfred R. Strecker [a]

[a] Institute of Geoscience, University of Potsdam, Campus Golm, Karl-Liebknecht-Str. 24-25, Potsdam, 14476, Germany
[b] Physics of Earthquakes and Volcanoes, GFZ Helmholtz Centre for Geosciences, Telegrafenberg, Potsdam, 14473, Germany
[c] Department of Earth and Environmental Sciences, University of Exeter, Penryn Campus, Penryn, TR10 9FE, UK
[d] Department of Physics and Astronomy, University of Bologna, Viale Berti Pichat 8, Bologna, 40126, Italy
[e] Department of Science, University of Roma Tre, Largo San Leonardo Murialdo 1, Rome, 00146, Italy

ARTICLE INFO

Editor: C. Lithgow-Bertelloni

Keywords:
Crustal unloading
Magma propagation
Analog experiments
Rift transfer zones
Along-rift volcanism
Off-axis volcanism

ABSTRACT

Volcanic activity between adjacent rift segments remains a critical, yet poorly understood aspect of volcano-tectonic processes in extensional regions. Here, we investigate how crustal stresses, particularly the interplay between tensional and unloading (removal of mass) stresses, influence magma propagation and the spatial distribution of volcanic centers in regions between spatially separate rift segments. Using the Copernicus Global Digital Elevation Model, we quantified asymmetries in crustal unloading and examined spatial correlations between volcanic centers and rift segment terminations in three exemplary study regions, including the Rhenish Massif (Germany), the Virunga Volcanic Complex (Western Branch of the East African Rift System), and the Adda'do Magmatic Segment (Southern Afar, Ethiopia). We additionally conducted experiments with analog materials to simulate the roles of hydrostatic and unloading stresses, as well as tensional stresses on magma trajectories. We found that magma pathways, and therefore the distribution of volcanic centers, are shaped by the competition between tensional and unloading stresses within and between separate rift segments. Minor extension and low-magnitude asymmetric crustal unloading result in scattered monogenic volcanoes (Rhenish Massif). Moderate extension and pronounced asymmetric rifting redirect magma laterally toward the tectonically less active, gentler side of half-grabens (Virunga Volcanic Complex). High extension rates and moderate rift asymmetry cause a concentration of both polygenic and monogenic volcanoes along rift axes (Adda'do Magmatic Segment). In all of these settings, diking constitutes a complementary mechanism, in addition to tectonic faulting, to accommodate regional extension.

1. Introduction

Crustal loading and unloading processes, driven by the addition or removal of surface mass, have a profound influence on crustal stresses in different geodynamic environments (Watts, 2001; Hooper et al., 2011; Brune et al., 2023). For example, regions affected by the build-up of ice sheets and their subsequent removal react to changes in loading, which can alter fault activity, by either promoting or suppressing seismic events (Grollimund and Zoback, 2001). This phenomenon is equally relevant in volcanically active regions, where crustal loading and unloading may control the orientation of magma-filled fractures (Anderson, 1937; Gudmundsson, 1986; Rivalta et al., 2019). The dynamic interplay between the evolution of topography, crustal loading and unloading, stress field, and magmatism is particularly well exemplified by tectono-magmatic processes associated with grabens and half-grabens, in the landscapes of extensional provinces (Olive et al., 2014; Brune et al., 2023).

Generally, the distribution of faults and volcanic activity in rifts follows predictable patterns. For example, volcanism typically aligns along the rift axis (hereafter, along-rift) during the early and late stages of extension (Ebinger and Casey, 2001; Corti, 2009; Keir et al., 2015). However, during intermediate stages of extension, volcanic features may also develop on the rift flanks (hereafter, off-axis volcanism), although the different mechanisms responsible are not always fully resolved and continue to be the subject of scientific debate (Bosworth, 1987; Maccaferri et al., 2014; Ferrante et al., 2024; Corti et al., 2025).

The early stages of rifting are characterized by a tensional stress regime with a vertically oriented maximum compressive stress (σ_1) and

* Corresponding author.
E-mail address: armeni@uni-potsdam.de (V. Armeni).

https://doi.org/10.1016/j.epsl.2025.119623
Received 27 April 2025; Received in revised form 19 August 2025; Accepted 3 September 2025

0012-821X/© 2025 The Author(s). Published by Elsevier B.V. This is an open access article under the CC BY license (http://creativecommons.org/licenses/by/4.0/).

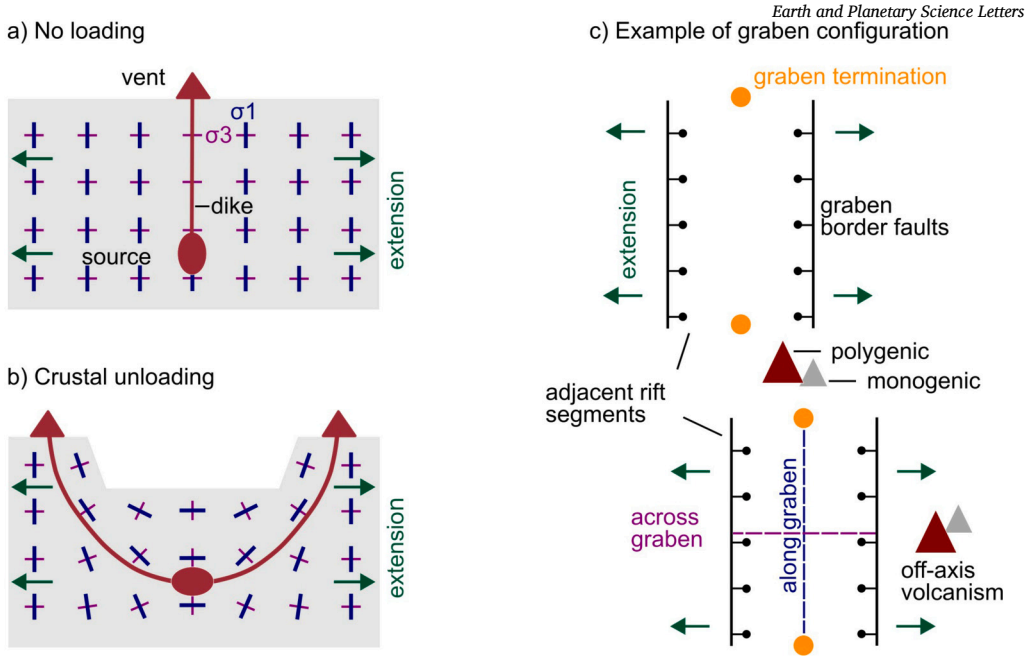

Fig. 1. Crustal stress field imposed by different gravitational loading scenarios in an extensional setting. Magma source (red ellipse) and dikes (solid red lines) align with the axis of greatest compression (σ_1; blue dashes) and are perpendicular to the axis of least compression (σ_3; magenta dashes). The orientations of the principal stress axes show the most likely magma propagation path. a) Below flat topography and under the influence of a far-field tensional stress field (green arrows), the main compressive stress axis (σ_1) is sub-vertical, and the least compressive stress axis (σ_3) is sub-horizontal. b) Topographic depression: unloading induced by mass removal causes a local rotation of the principal stress axes resulting in a sub-horizontal (σ_1) and sub-vertical (σ_3) below the graben, with (σ_1) becoming progressively sub-vertical and (σ_3) sub-horizontal towards the flanks of the structure, modified from Acocella et al. (2024). c) Schematic model of graben setting with along-strike terminations (orange circle) and the spatial distribution of volcanoes (red and gray triangles) between neighboring rift segments, as well as in off-axis locations.

a sub-horizontally oriented axis of least compression (σ_3) (Fig. 1a). Such a setting promotes the formation of fractures and normal faults, as well as the vertical ascent of magmas in dikes and associated aligned eruptive centers at the surface (e.g., Anderson, 1937; Nakamura, 1977). As rifting progresses, normal faulting and continued graben formation result in focused mass reduction (unloading), which causes the rotation of the principal stress axes in the crust (Maccaferri et al., 2014; Ferrante et al., 2024). While the graben is subsiding, σ_3 becomes sub-vertical beneath it, transitioning into a sub-horizontal orientation toward the rift flanks (Fig. 1b; Maccaferri et al., 2014; Ferrante et al., 2024).

Both scenarios explain the spatial distribution of volcanic edifices along the rift axis as well as in off-axis locations. However, a rift system typically consists of different segments, with graben- or half-graben geometries, and the axis of these segments may be laterally offset (Fig. 1c). Such a configuration results in semi-independent structural and magmatic entities and associated depositional environments, whose along-strike termination may develop transfer zones that accommodate extension between segments (e.g., Rosendahl, 1987); these transitional areas may host large polygenic stratovolcanoes (e.g., Nyiragongo and Nyamuragira in the East African Rift; Ebinger et al., 1991), monogenetic volcanic fields (e.g., Eifel volcanic field, Rhenish Massif; Schmincke, 2004), and calderas (e.g., Okataina, New Zeland; Seebeck and Nicol, 2009).

Whereas the possible mechanisms of along- and off-axis volcanism have been well documented by structural studies (Bosworth, 1987; Ebinger and Casey, 2001) and various modeling efforts (Olive et al., 2014; Maccaferri et al., 2014; Oliva et al., 2022; Ferrante et al., 2024), the nature of volcanic processes between adjacent rift segments is known to a lesser extent and has been less explored (Pollard and Aydin, 1984; Corti et al., 2003; Keir et al., 2015; Muirhead et al., 2015). In particular, an unsolved key question concerns what controls magma transport in these transition zones, which are characterized by less pronounced extension and decompression melting. To contribute to a better understanding of the volcano-tectonic evolution of such regions, we analyzed the pattern of volcanism and potential stress perturbations in the transition between spatially separated grabens. Specifically, we first conducted an analysis of Digital Elevation Models (DEM) of three exemplary, although different, extensional systems that are characterized by both along- and off-axis rift volcanism. The DEM analysis aimed at quantifying the geometric and volumetric characteristics of the grabens. The analyzed regions include the Rhenish Massif in Germany (Fig. 2a, c), the Virunga Volcanic Complex in the Western Branch of the East African Rift System (Fig. 2b, d) and the Adda'do Magmatic Segment of Southern Afar (Fig. 2b, e). In a second step, we designed analog experiments to simulate how various stress states affect magma pathways between rift segments. By investigating the influence of tectonic and topography-related stresses on magma transport, we focus on the important role of tectonic unloading in influencing the spatial patterns of volcanism between adjacent rift segments.

2. Regional examples

We selected three continental rift examples because they span two orders of magnitude of long-term tectonic and geodetic extension rates and an order of magnitude of crustal unloading, with graben depth as a proxy for unloading. At the lower end of extension rates, and with a rate of 0.07 mm/yr, is the Lower Rhine Graben (Camelbeeck et al. 2020; Fig. 2a, c). With approximately 2 mm/yr of extension the Virunga Volcanic Complex represents an intermediate case (Saria et al. 2014; Fig. 2b, d), whereas the upper end of extension-rate values is represented by 5 mm/yr observed in the Adda'do Magmatic Segment (Saria et al. 2014; Fig. 2b, e).

2.1. Volcanism in the Rhenish Massif

Volcanism in the Rhenish Massif, including the Siebengebirge, Westerwald, Hocheifel, and the Eifel volcanic fields, occurs at the southern termination of the Lower Rhine Graben (LRG), which is an integral part of the northwestern Rhine Graben Branch (Fig. 2c) within the European Cenozoic Rift System (Ziegler 1992; Fig. 2a). Whereas extension in

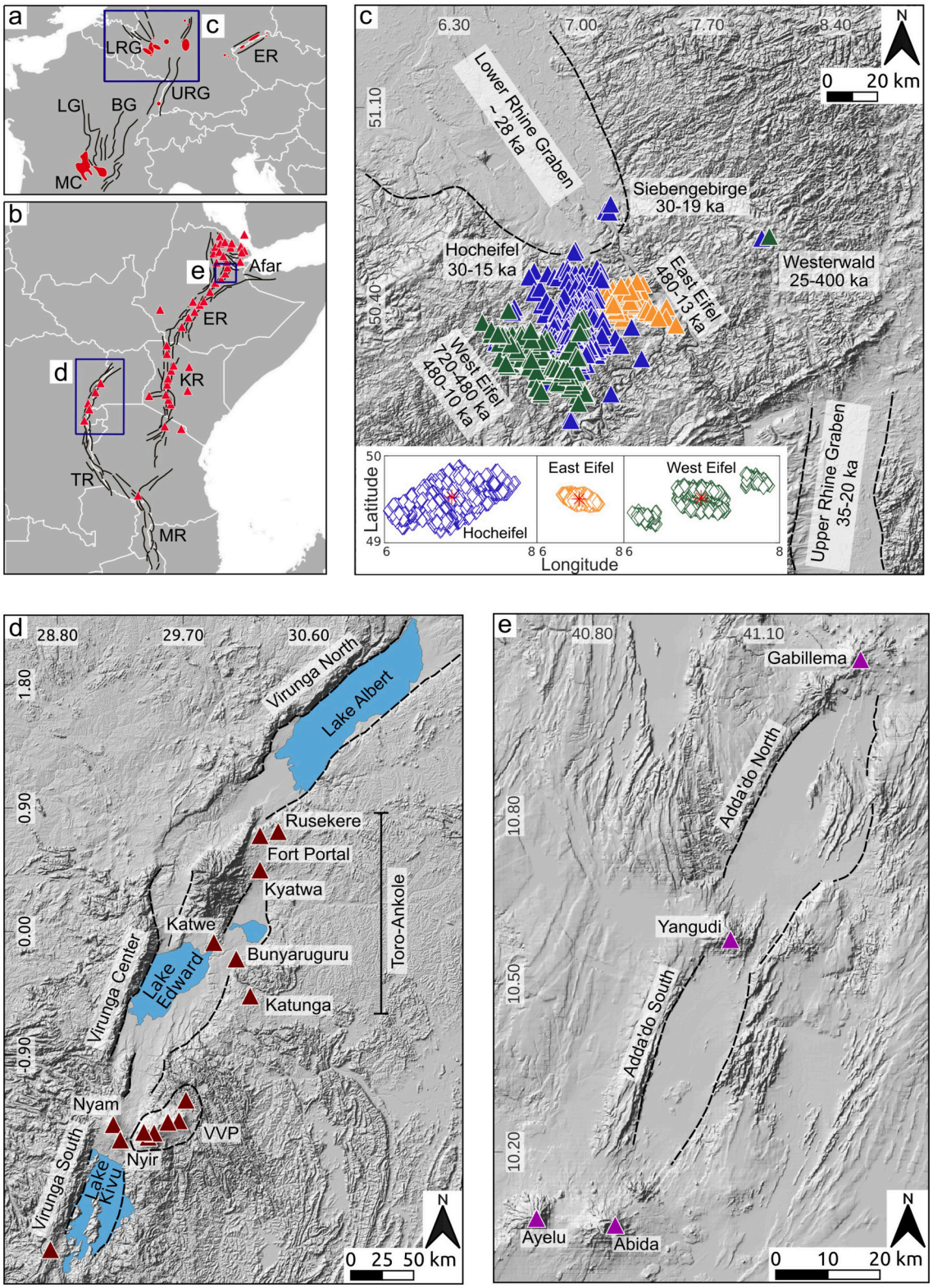

Fig. 2. Examples of volcanism in extensional settings. a) European Cenozoic rift system (ECRIS). MC: Massif central; LG: Limagne Graben; BG: Bresse Graben; LRG: Lower Rhine Graben; URG: Upper Rhine Graben; EG: Eger Graben. The blue rectangle is the Rhenish Massif (RM), illustrated in more detail in (c). b) East African Rift System (EARS). ER: Ethiopian Rift; KR: Kenya Rift; TR: Tanganyika Rift; MR: Malawi Rift. Blue rectangle outlines the Virunga Volcanic Province (VVP), shown in (d), and the Adda'do Magmatic segment (AMS), shown in (e). In all panels, red spots and triangles are volcanic provinces and centers, respectively. The volcanic vent locations are from the Smithsonian catalog (Global Volcanism Program et al., 2024), and for the Rhenish Massif, these were further implemented using digital mapping techniques. Black-dashed lines mark rift borders. c), d), and e) Copernicus 90 m shaded relief maps showing the volcano-tectonic architecture of the selected rift systems. Inset in panel (c) shows the main spatial distribution of volcanic centers in the Rhenish Massif. S: Siebengebirge; H: Hocheifel; W: Westerwald; WE: West Eifel, and EE: East Eifel.

the Upper Rhine Graben began in the late Eocene, rifting in the Lower Rhine Graben started in the late Oligocene (Geluk et al., 1994). The latter comprises a series of NW-SE-oriented half-grabens that extend approximately 100 km in length and up to 50 km in width, narrowing as they approach the Rhenish Massif. The Tertiary and Quaternary basin fill reaches a maximum thickness of up to 2000 m on the western side of the graben, gradually thinning to approximately 130 m on the eastern side (Schäfer et al., 2005).

The Siebengebirge region (Fig. 2c), experienced volcanism between approximately 30 and 19 Ma (Schubert et al., 2015), likely associated with regional rifting (Kolb et al., 2012). The Westerwald records volcanic activity from 28 to 22 Ma (Fig. 2c), with a later phase between 800 and 400 ka (Lippolt, 1983). Both regions share a main volcanic phase at approximately 25 Ma (Schubert et al., 2015). The Hocheifel, between the East and West Eifel volcanic fields (Fig. 2c), records volcanic activity from approximately 44 to 24 Ma (Lippolt, 1983); this has been interpreted as the continuation of pre-rift volcanism in the northern Upper Rhine Graben that propagated northwestward (Fekiacova et al., 2007).

The manifestations of Quaternary volcanic activity are concentrated in the West and East Eifel volcanic fields (Fig. 2c). The West Eifel experienced main periods of volcanic activity during the middle Pleistocene (ca. 720–480 ka) and the late Pleistocene (ca. 80–10 ka). During the period of interrupted activity in the West Eifel, the East Eifel became active (ca. 480–13 ka), culminating in the Laacher See Plinian eruption at 12,880 years BP (Schmincke, 2004).

2.2. Volcanism in the Western Branch of the East African Rift System

The Western Branch of the East African Rift consists of a series of differently oriented, segmented asymmetric grabens (Fig. 2d), i.e., the Albert, Edward, and Kivu basins, which are separated by transfer zones (Ebinger et al., 1991). The along-axis segmentation includes a shift in orientation, from NE-SE in the Kivu and Edward Rifts, to ENE-WSW in the Albert Rift (Upcott et al. 1996; Fig. 2d). The onset of rifting is debated; Ebinger et al. (1991) suggested a mid-Miocene initiation in the central section, spreading north (12 Ma) and south (7 Ma), while Roberts et al. (2012) proposed an earlier start at 25 Ma, contemporaneous with some sectors of the Eastern Branch. The half-grabens are approximately 150 km long and 40–70 km wide, with volcanism (Fig. 2d) mainly occurring during the last 11 Ma (Ebinger and Casey, 2001; Acocella, 2021). In the Western Branch, depth to pre-rift basement and rift flank topography vary between 1–8 and 1–2 km, respectively, with basin depth generally correlating with rift flank elevation (Karner et al., 2000). Volcanic activity is restricted to the South Kivu (21 Ma), Virunga (first episode at 12.6 Ma) (Pouclet et al., 2016), and Toro-Ankole (50-10 ka) volcanic provinces (Boven et al., 1998). The Virunga Volcanic Complex (Fig. 2d), between the Kivu and Edward rifts, consists of eight main volcanic edifices, including the Nyamuragira and Nyiragongo polygenic volcanoes.

2.3. Volcanism in Southern Afar

The region between Afar and the Main Ethiopian Rift hosts NNE-SSW-striking, right stepping en-échelon rift segments of Miocene age (Keir et al., 2006). The rift basins are commonly about 60 km long and 20 km wide, accommodating over 80% of extension (Ebinger and Casey, 2001; Acocella, 2021). An example is the Adda'do Magmatic Segment (Fig. 2b, e), composed of two oval-shaped grabens, here referred to as the Northern and Southern Adda'do sub-rifts, whose depth is not explicitly known. At the northern termination of the Adda'do North graben is the Gabillema volcanic complex. In the middle part of the Adda'do graben, halfway between Abida and Gabillema, is the Yangudi volcano. At the southern termination of the Adda'do South graben are the Abida and Ayelu eruptive centers. While Gabillema, Yangudi, and Abida are in an along-axis position, Ayelu is laterally offset (Rees et al., 2023). South from Ayelu, the Afar depression grades into the northern Ethiopian Rift, with the active axis located a few tens of kilometers westward (Varet, 2017).

3. Methods

3.1. DEM analysis

We used the 90-meter resolution Copernicus Global Digital Elevation Model (COP90 DEM) to quantify the geometric and volumetric characteristics of the grabens. Given the regional scale of the study area (tens to hundreds of kilometers), this resolution offers an effective compromise between spatial coverage and processing efficiency (Purinton and Bookhagen, 2017). We calculated hillshade (Fig. 2), slope, and 1-km-radius relief maps (see Supplementary material) to identify the graben terminations. We measured the radial distance of the volcanic centers from the nearest termination (Table 1 in Supplementary material).

To quantify the geometric and volumetric characteristics of the grabens, we generated a new DEM representing the pre-rift topography (Fig. 3). We manually identified the graben area and removed it from the original COP90 DEM. Next, we applied a 5-km buffer along the graben boundary and used linear triangle interpolation. We experimented with different interpolation methods, including higher-order splines and polynomials, and found that linear interpolation provided the results that most closely matched published geological data (references in Section 2).

On the interpolated DEM, swath profiles were traced with specified dimensions: 10 km width and 120 km length for the Virunga region (Fig. 3a); 10 km width and 36 km length for Adda'do (Fig. 3b); and 10 km width and 132 km length for the Lower Rhine Graben (Fig. 3c). In all swaths, the center is the reference point and computations are made moving outward toward the lateral extremities of the swath. Within these profiles, we calculated the following parameters: (1) graben depth, which refers to the elevation difference between the center and the flanks of the graben (Fig. 3). This value is a measure of subsidence accommodated by the graben, and it is a lower bound for the total amount of subsidence as it does not account for any sedimentary basin fill; (2) cumulative missing volume, which refers to the total volume of material displaced from the graben due to its subsidence. For each segment, the volume is estimated by multiplying the graben depth by the width of the swath and the horizontal distance between adjacent sampling points for every swath; (3) elevation difference, which defines the absolute difference in maximum elevation between the flanks of the graben and the spatial variation of topography. The topographic analysis and serial swath profiles were conducted in Matlab using TopoToolbox (Schwanghart and Scherler, 2014) and the TAK toolbox (Forte and Whipple, 2019).

3.2. Analog experiments

Following Mantiloni et al. (2021), we conducted experiments using gelatin and air as analogs for the crust and magma, respectively. Details on gelatin preparation, Young's modulus measurements, and injection sequences are provided in the Supplementary material. We present five experiments designed to explore how air-filled cracks (dike analog) respond to different stress states: hydrostatic (Setup 1, 2; Fig. 4a, b), tensional (Setup 2, 3, 4; Fig. 4b, c, d), and spatially reduced hydrostatic stresses (Setup 3, 4, 5; Fig. 4c, d, e). In all experiments except Setup 1, the right-hand stress configuration differs from the left-hand side (Fig. 4a-e).

Hydrostatic stress (Setup 1, 2; Fig. 4a, b) was generated under a flat surface and without strain on the boundaries. This allowed observing the behavior of air-filled crack trajectories under simple stress conditions and evaluating inhomogeneities in the gelatin that might influence the experiments.

Tensional stress (Setups 2, 3, 4; Fig. 4b, c, d) was induced by removing two plastic plates on the long sides of the container (width: 40 cm,

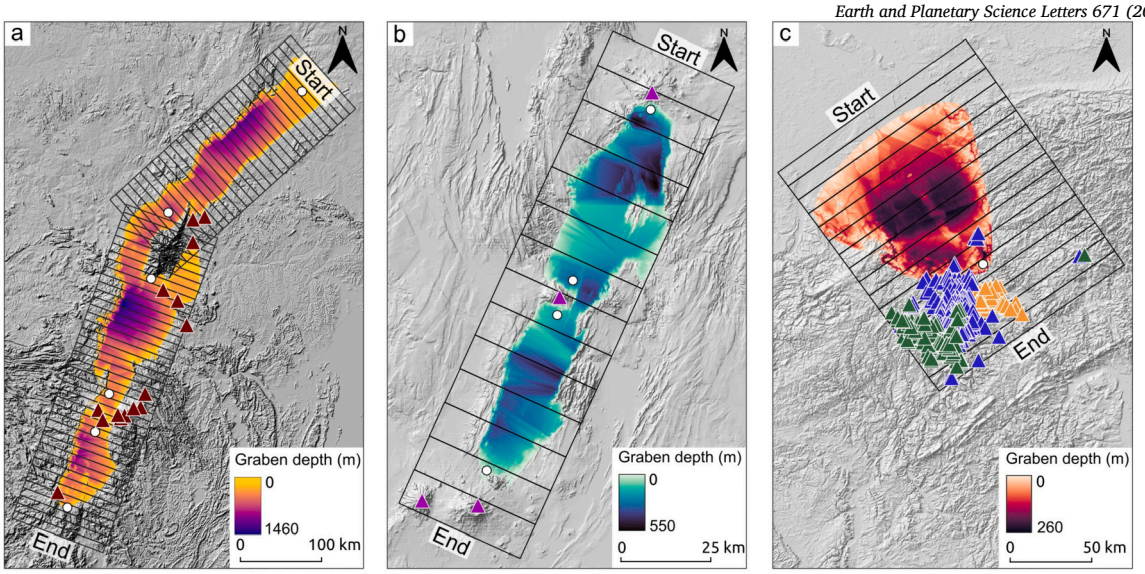

Fig. 3. Graben-depth interpolations for (a) the Western Branch of the East African Rift System, (b) the Adda'do Magmatic Segment, and (c) the Lower Rhine Graben. Black boxes indicate serial swath profiles shown in Fig. 5, white circles mark the graben terminations, and triangles represent volcanic vents (identical color scheme as Fig. 2).

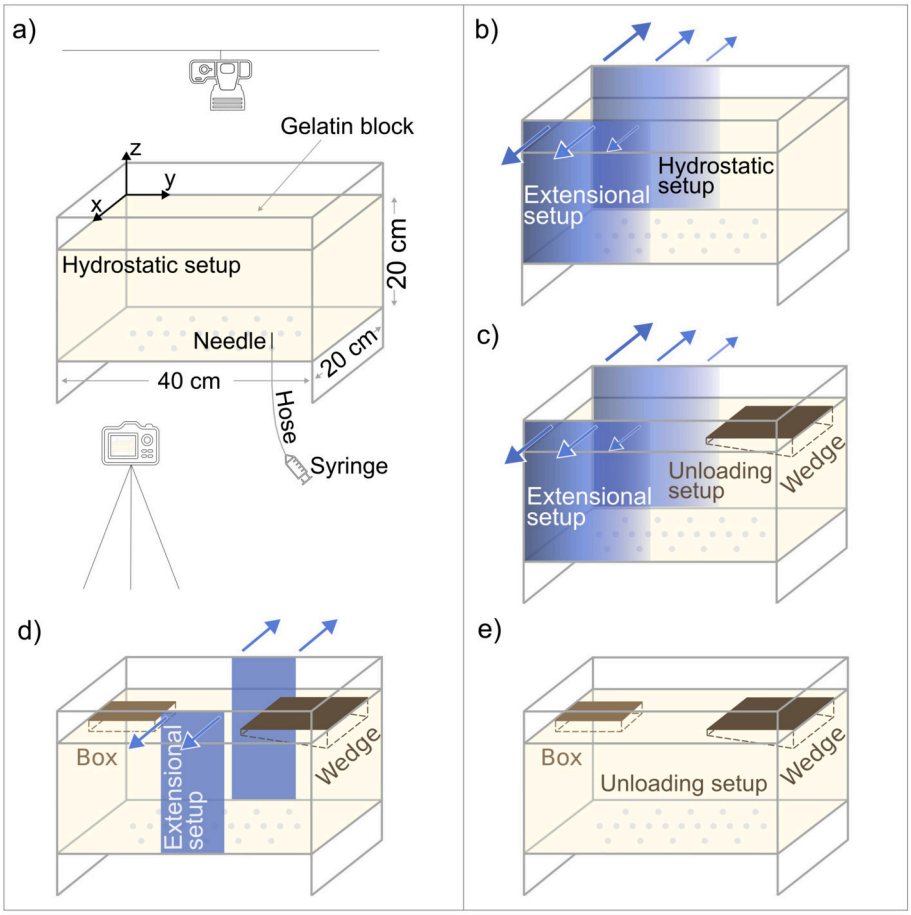

Fig. 4. Experimental setups. a) Schematic view of the box containing the gelatin block. Air is injected through the holes (light-gray circles) at the bottom of the container. Setup 1: flat topography under hydrostatic stress conditions. b) Setup 2: flat topography under hydrostatic vs. tensional stresses. c) Setup 3: wedge-shaped unloading vs. tensional stresses. d) Setup 4: box- and wedge-shaped unloading vs. tensional stresses. e) Setup 5: box- and wedge-shaped unloading without tensional stresses.

height: 35 cm, thickness: 2.8 ± 0.1 mm). This resulted in differential extension from the center towards the edges of the container, as the plate edges bent the movable inner wall of the box. Two larger plates (width: 20 cm; height: 35 cm, thickness: 2.7 ± 0.1 mm) were used in Setup 2 and 3, while two smaller plates (width: 10 cm, height: 35 cm, thickness: 2.9 ± 0.1 mm) were used in Setup 4, generating two different stress magnitudes.

A spatially confined reduction of the hydrostatic stress, or unloading (Setup 3, 4, 5; Fig. 4c, d, e), was produced by imposing wooden molds on the gelatin surface. We used two mold shapes: a box (width: 6 cm; length: 14 cm, thickness: 3 cm; Fig. 4d, e) and a wedge (width: 10 cm; length: 14,5 cm; thickness: from 4 to 1.2 cm; Fig. 4c, d, e). Molds were covered with tape to prevent gelatin absorption and removed before the injections, leading to surface unloading. In Setup 4 (Fig. 4d), we removed both plates and molds simultaneously. This design allowed us to observe how the trajectories behave under the more complex stress scenario of simultaneous tensional and unloading stresses. In Setup 5 (Fig. 4e), no tensional stress was applied.

3.3. Scaling of the analog experiment

Geometric, dynamic, and kinematic similarity criteria ensure that analog models are properly scaled to natural systems (Hubbert, 1937). Here, we assess how upscaling is handled in our setup, focusing on the relevant stress and length scales that control dike propagation in extensional settings. Geometric similarity prescribes proportional length scales and angles between model and nature. A key length scale in magma transport is the buoyancy length L_b (e.g., Merle, 2015; Mantiloni et al., 2021):

$$L_b = \left(\frac{K_c}{\sqrt{\pi}\Delta\rho g} \right)^{2/3} \tag{1}$$

where K_c is the medium fracture toughness, $\Delta\rho$ is the density contrast between the host medium and the injected fluid, and g is acceleration due to gravity. Common values in nature are $\Delta\rho_r = 100$ kg m^{-3}, $K_c^r = 0.2$ to $1 \cdot 10^9$ Pa m$^{1/2}$ as the effective rock fracture toughness for the propagation of km-scale dikes (e.g., Rivalta et al., 2015; Konstantinou, 2024) and $E = 10 \cdot 10^9$ to $10 \cdot 10^{10}$ Pa as the Young's modulus (Fossen, 2016). In our experiments, $\Delta\rho_{gel} = 1000$ kg m^{-3} and $K_c^{gel} = 40 - 60$ Pa m$^{1/2}$ for a gelatin with Young's modulus in the range $E = 1000 - 2000$ Pa (Kavanagh et al., 2013). We obtain $L_b^* = 2.5 \cdot 10^{-6}$ to $10 \cdot 10^{-6}$, where the $*$ indicates model-to-nature ratio. The mold dimensions scale to natural rift widths of 6 – 70 km and depths of several kilometers, consistent with sectors of the East African Rift (40 – 70 km width, 1.5 km depth), Adda'do (10 – 20 km width, 1 km depth) and Lower Rhine Graben (10 – 40 km width, up to 2 km depth). While natural rift-segment lengths range from 50 to 150 km, the shorter mold length constrained by box size does not affect our results because we consider the mold length to represent half of the natural rift length.

Dynamic similarity requires that stresses in nature and the experiments have similar ratios. The unloading stress ratio, σ_u^*, is:

$$\sigma_u^* = \frac{\sigma_u^{gel}}{\sigma_u^{rock}} \tag{2}$$

where $\sigma_u = \rho g h$. Taking $\rho_r = 2500$ kg m^{-3} for shallow basement rock layers in rift zones, $h_{gel} = 1.2 - 4$ cm and $h_r = 0.4 - 2$ km as the effective depth of the depression for our experiments and in nature, we obtain $\sigma_u^* = 2.4 \cdot 10^{-6}$ to $4 \cdot 10^{-5}$. We ensure that other characteristic stress ratios fall within the same order of magnitude as σ_u^*. We first evaluate the ratio between the stress induced in the gelatin mass by lateral strain (σ_{yy}) and the stress due to regional extension (σ_t):

$$\sigma_t^* = \frac{\sigma_{yy}}{\sigma_t} \tag{3}$$

The lateral strain in the extended portion of gelatin is derived by solving Hooke's equation after imposing the boundary conditions of our experiments. Considering a lateral strain $\Delta b/b_0 = 0.27$ along the short box side and $\Delta a/a_0 = 0$ along the long side, and considering that the upper gelatin surface is free of imposed stresses, we obtain from Hooke's law:

$$\sigma_{yy} = \frac{E}{1-\nu^2}\frac{\Delta b}{b_0} \tag{4}$$

For rift settings, we assume regional tensional stresses in a range of 1 to 5 MPa (see discussion by Ferrante et al., 2024), resulting in $\sigma_t^* = 1.6 \cdot 10^{-6}$ to $5 \cdot 10^{-6}$. We also scale buoyancy pressure in fluid-filled cracks, $\sigma_b = \Delta\rho g L$ (Namiki et al., 2019), that competes with unloading stresses in controlling crack trajectories (Watanabe et al., 2002; Maccaferri et al., 2019). In the experiments, we use $\Delta\rho = 1000$ kg m^{-3} and $L_{crack} = 4 \cdot 10^{-2}$, so that $\sigma_b = 400$ Pa. In nature, assuming $\Delta\rho = 400$ kg m^{-3} and $L_{dike} = 5 \cdot 10^3$, $\sigma_b = 2 \cdot 10^7$ Pa, yielding a buoyancy pressure ratio of $\sigma_b^* = 2 \cdot 10^{-5}$. Together, these dimensionless stress ratios (σ_u^*, σ_t^*, and σ_b^*), fall within the accepted range for properly scaled analog models (e.g., Kavanagh et al., 2013; Merle, 2015; Mantiloni et al., 2021). Although we do not address kinematic similarity (time and viscosity), our scaling confirms that the experimental setup satisfies the key similarity criteria for dike and rift-scale processes, ensuring that dike propagation observed in our experiments can be compared to the formation of dikes in natural rift systems.

4. Results

4.1. DEM analysis

The DEM analysis for 471 volcanic vents across the three study areas, including 452 in the Rhenish Massif, 15 in the Western Branch of the East African Rift System, and four in the Adda'do Magmatic Segment, provides insights into how volcanic centers are spatially distributed in relation to rift geometry.

In the Rhenish Massif, the radial distances of vents from the southeastern termination of the Lower Rhine Graben range from 10 to 70 km. The nearest vents to the termination belong to the Paleogene volcanic fields of the Siebengebirge and Hocheifel, whereas the Quaternary eruptive centers are farther away (Fig. 2c). The interpolated graben depth ranges from 0 to 266 m and exhibits southeastward-dipping depocenters (Fig. 3c). The cumulative missing volume (Fig. 5d) is asymmetric for most of the graben axis but approaches zero toward the graben terminations. The maximum elevation differences along the graben are small and typically below 100 m (Fig. 5d). Slightly higher values are observed at the southeastern termination, corresponding to the graben depocenter. The majority of the vents are densely distributed south of the graben termination.

In the Western Branch of the East African Rift System, the radial distances of volcanic centers from the graben terminations vary, with most volcanic activity occurring between the rift segments (Fig. 2d). Examples include Katwe (20 km from the nearest graben termination), Nyiragongo (18 km), and Nyamuragira (24 km). A few centers are situated on the graben flanks but are relatively close to their terminations, such as in the Virunga Province. Katunga is the most distant volcano with respect to the graben termination (72 km) and axis (60 km). The interpolated graben depths range from 0 to 1465 m, with westward-dipping depocenters observed in the Kivu, Edward, and Albert rifts (Fig. 3a). The cumulative missing volume and elevation difference along the graben axis are strongly asymmetric. Maximum elevation differences exceed 500 m in the northern Edward and central Albert rifts and decrease towards the rift terminations (Fig. 5a, c). The spatial distribution of these values closely mimics the arc-shaped configuration of the Virunga and Toro-Ankole volcanic provinces and asymmetry of the Edward Rift (Fig. 3a). Moreover, those regions of the graben with the greatest missing volume and elevation differences are associated with fewer volcanic

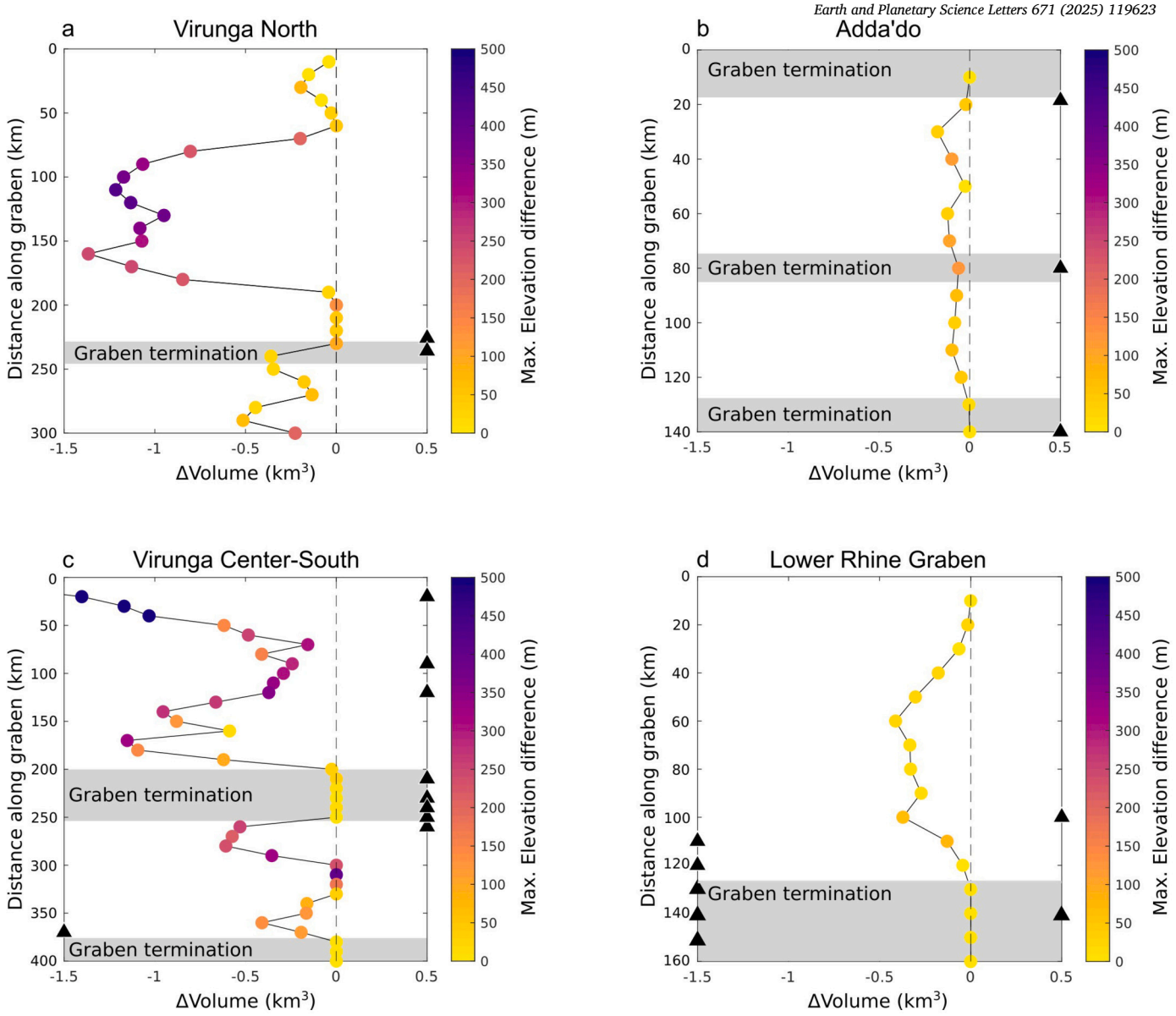

Fig. 5. Asymmetry of the missing volume of the graben depression relative to the graben axis in the selected study regions: a) Virunga North, b) Adda'do Magmatic Segment, c) Virunga Center and South, and d) Lower Rhine Graben. For each swath profile (traces shown in Fig. 3), the asymmetry of the volume of missing material in the graben is estimated and color-coded based on the elevation difference at the corresponding location. Gray rectangles are graben terminations. Black triangles represent volcanic vents, illustrating their spatial distribution on the western or eastern side of the graben axis.

centers (darker colors in Fig. 5a, c), which are predominantly located on the graben flanks. In contrast, volcanic centers become more frequent and closely spaced near the graben terminations.

In the Adda'do Magmatic Segment, the Gabillema, Yangudi, and Abida volcanoes are located at the terminations of the grabens and along the rift; an exception is Ayelu, which is slightly offset but still close to the graben termination (15 km) (Fig. 2e). The interpolated graben depths range from 0 to 557 m associated with eastward-dipping depocenters (Fig. 3b). The cumulative missing volume along the graben axis is asymmetrical and decreases toward the terminations of the graben segments (Fig. 5b). Maximum elevation differences along the graben axis are generally below 200 m (Fig. 5b). No volcanic features are observed within the grabens and on their flanks.

Overall, the study reveals that volcanic centers preferentially form near segment terminations or along one side of the rift, despite regional differences in graben depth, depocenter orientation, and radial distances of vents from graben terminations. Near the graben terminations, where missing volumes are minimal ($\lesssim -0.5\,\mathrm{km}^3$), volcanic centers are typically smaller and more frequent and closely spaced (i.e., Siebengebirge, Fig. 2c, Fig. 5c). For missing volumes in the range -0.5 km^3 to -1 km^3, volcanism is sparse and mainly located on the graben flanks (i.e., Katunga, Fig. 2d, Fig. 5b). When the graben attains significant depth, corresponding to missing volumes exceeding $\gtrsim 1\,\mathrm{km}^3$, volcanic activity disappears within the rift, as well as on the graben flanks (e.g., Albert Rift, Fig. 2d, Fig. 5a).

4.2. Analog experiments

Under hydrostatic stress conditions (Setup 1 and 2; Fig. 6a-c1 and b-c2), cracks tended to propagate sub-vertically following the strike of the injection with dip angles of approximately 70° (Fig. 6a1, c1, c2). In map view, the crack trajectories generally maintained the same spacing compared to the injection points (Fig. 6b1, b2).

In the case of tensional stress conditions (Setup 2 and 3; Fig. 6a-c2 and a-c3), cracks tended to align along the axis of the gelatin box, perpendicular to the least-compressive stress axis, σ_3. Cracks injected

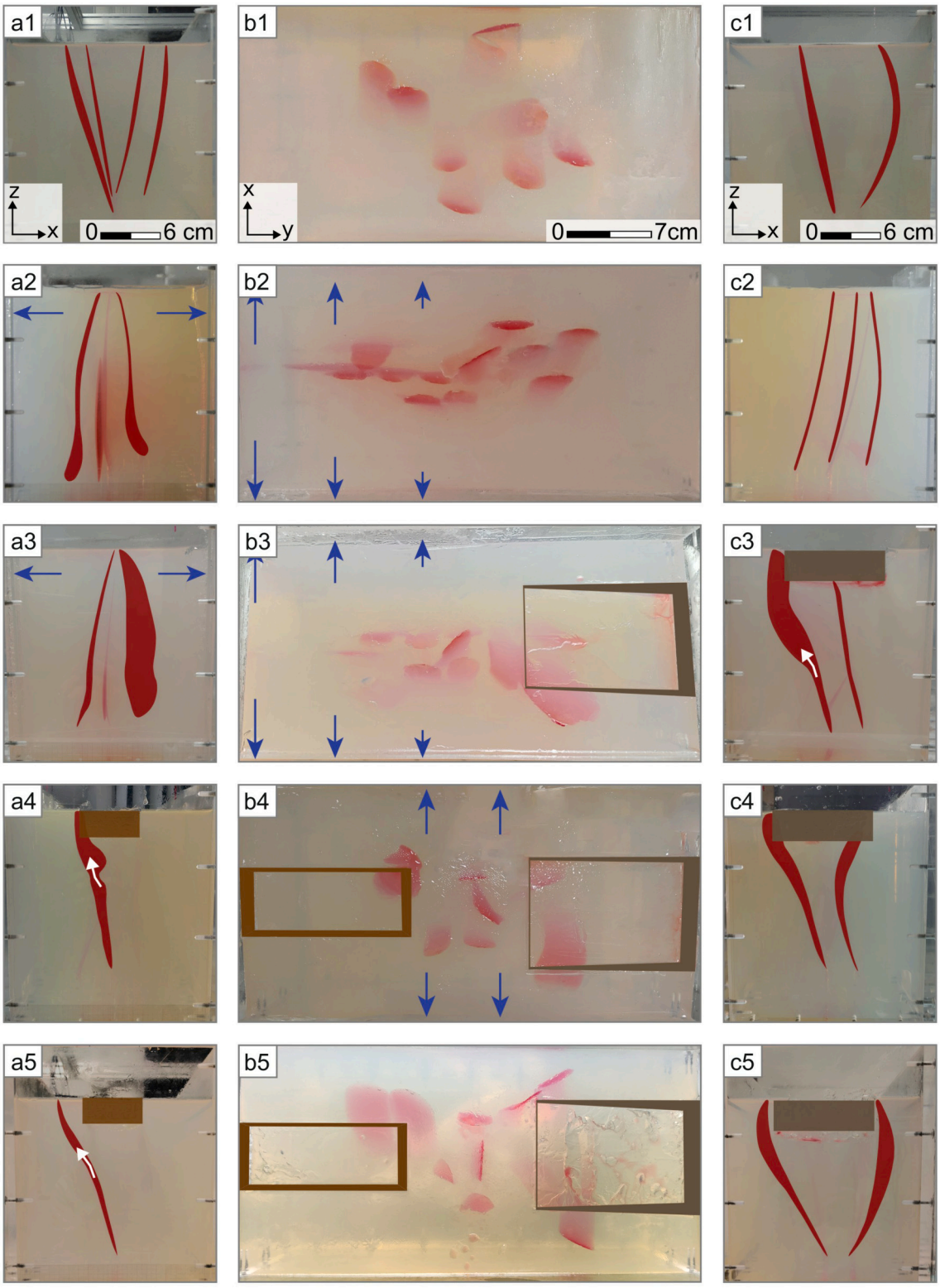

Fig. 6. Analog results: along strike views (a1-5; x - z plane, left side of the box, and c1-5; x - z plane, right side of the box), and map view (b1-5; y - x plane), of air-filled crack trajectories after the experiments. The length of the blue arrow is proportional to the resulting amount of extension of the gelatin block. Brown colored areas represent the location of the molds, whereas red lines highlight crack trajectories. The white arrow indicates the deflection point of the trajectories. The numbering of setups corresponds to that in Fig. 4: Setup 1, (a1, b1, c1) flat topography under hydrostatic stress conditions. Setup 2, flat topography under hydrostatic (b2, c2) vs. tensional stresses (b2, a2). Setup 3, wedge-shaped unloading (b3, c3) vs. tensional stresses (b3, a3). Setup 4, box- and wedge-shaped unloading (a4, b4, c4) vs. tensional stresses (b4). Setup 5, box- and wedge-shaped unloading (a5, b5, c5) without tensional stresses. See also video S1 and S2 in the Supplementary material.

from the lateral grid of holes at the bottom of the box converged towards the center of the box on the surface (Fig. 6a2, a3). The map view shows an en-échelon crack pattern (Fig. 6b2, b3).

By applying box- or wedge-shaped unloading conditions, the reduction of overburden (Setup 3, 4, 5; Fig. 6b3, b4, b5) generated substantial modifications in the air-filled crack trajectories. Initially, the cracks propagated sub-vertically, but subsequently, they were deflected and twisted away from the rift-like depression, propagating either to the flanks of the depression or towards its termination. The deflection resulted in cracks propagating over a significant lateral distance beneath the mold before emerging at the gelatin surface. In the along-strike view, the deflection points corresponded approximately to the width of the rift-like depression (Fig. 6c3, a4, c4, a5, c5). In map view, the final configuration of the cracks in both the box- and wedge-shaped unloading cases appeared to be similar (Figs. 6b3, b4, b5). However, the degree of deflection of the trajectories and the distance from the rift termination at which the cracks reached the surface varied between experiments with box- and wedge-shaped geometries. When the rift-like depression had a box-shaped geometry, the trajectories tended to propagate subhorizontally and followed a longer path below the depression (Fig. 6a4, b4, a5, b5). In contrast, with a wedge-shaped geometry, the deflection of the trajectories was smoother and arcuate (Fig. 6b3, c3, b4, c4, b5, c5), resulting in a shorter path. Interestingly, oblique orientations of analog fissures were observed in Setup 4 despite σ_3 being perpendicular to the long axis of the experimental box (Fig. 6b4). Such fissures were also generated in Setup 5 (Fig. 6b5), without imposing a tensional stress field.

4.3. Spatial trend in volcanic clustering across natural and analog rifts

A consistent distribution of volcanic centers emerged from both the DEM-based analysis of natural rift systems and the results of the analog experiments: volcanism preferentially occurred near rift/mold segment terminations (orange bars in Fig. 7a, b), progressively shifting from within the rift/mold (yellow bars) to the flank (blue bars) as the distance from the termination increased and the graben deepened.

Air-filled cracks that reached the surface at the terminations of the mold were supplied from any injection point beneath the mold (Fig. 7c). In contrast, air-filled cracks that opened on the flanks of the mold were injected from the central row of holes below the mold. The only crack reaching the surface within the mold was injected from a lateral row of holes (inset in Fig. 7). See Supplementary material and Fig. S3 for further details.

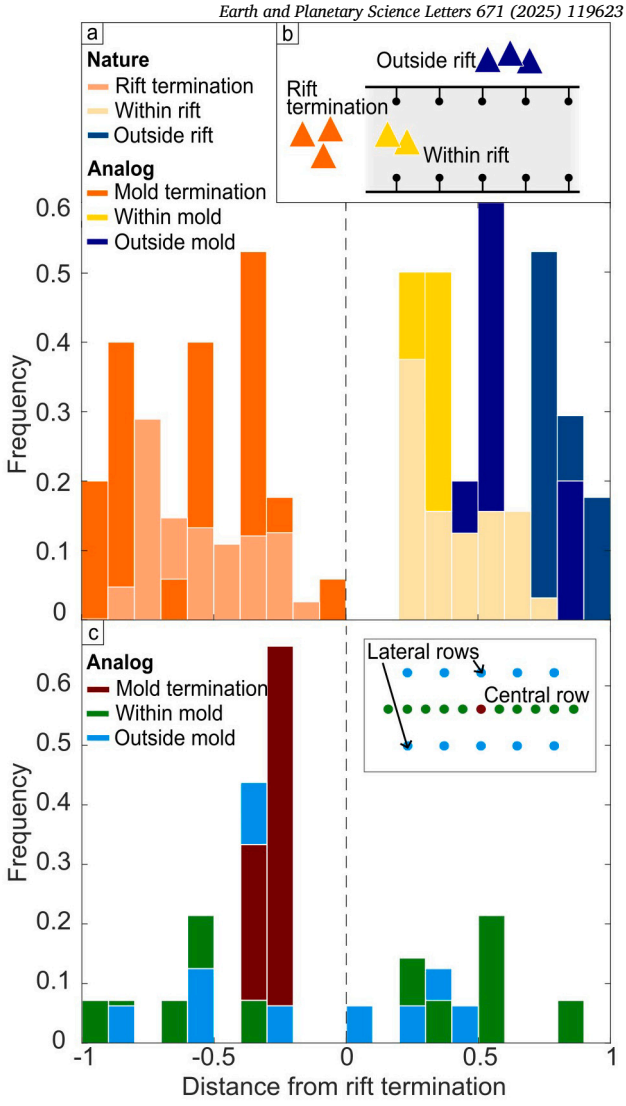

Fig. 7. a) Histogram showing the radial distance of volcanic vents from the graben termination, normalized to the graben/molds width, for both natural and simulated cases. The distance from the termination is positive if the vents are within or on the flanks of the rift/molds; the values are negative if the vents are in the termination area. b) Schematic representation of vent locations relative to the graben. c) Histogram illustrating the spatial distribution of air-filled crack trajectories, color-coded by their injection point. The inset in (c) shows a schematic view of the bottom of the gelatin box and the holes used for air injection.

5. Discussion

5.1. Caveats: assumptions and limitations of DEM analysis and analog experiments

Rift segments develop through complex geological histories involving multiple phases of deformation and changes in the tectonic stress field, magmatism, and the presences of lithological heterogeneities (e.g., Haug and Strecker, 1995; Ebinger and Casey, 2001; Olive et al., 2014; Muirhead et al., 2015). Inherited crustal fabrics, for instance, can influence the localization of rift basins, fault growth and vent migration (e.g., Corti et al., 2003; Brune et al., 2023). We acknowledge all of these factors, but in our approach we did not aim to replicate the full geological evolution of the study areas. Instead, our approach isolates the primary control on magma transport using a simplified, yet reproducible combination of topographic analysis and analog experiments.

The DEM analysis provides a snapshot of the present-day tectonomagmatic system and does not capture the dynamic evolution of the rift and volcanic activity over time. Accordingly, the use of linear interpolation to estimate the geometric and volumetric characteristics of the graben is a first-order approximation that may oversimplify a complex geological feature. Linear interpolation is widely used in regional-scale studies (e.g., Rees, 2000; Wang et al., 2015) because it provides an estimate of subsidence and basin geometry in areas where geophysical constraints (e.g., data from seismic reflection profiles or well information) are limited or unevenly distributed. The interpolated results were validated against the outcomes of prior studies (Ebinger et al., 1991; Geluk et al., 1994; Karner et al., 2000; Schäfer et al., 2005), which confirm that the approach chosen here reliably reproduces the principal rift geometries. A further advantage in the chosen approach is the computational efficiency, which does not compromise the quality of the results. For a similar reason, we selected a DEM with 90-meter-resolution, which captures first-order rift morphologies while minimizing artifacts unrelated to rift architecture and maintaining sufficient pixel density for solid analysis (Purinton and Bookhagen, 2017; Amatulli et al., 2020). However, this only approximates load changes or erosion. For instance, the reduced density contrast between sediment infill and basement rocks is not accounted for, thus potentially underestimating mass redistribu-

tion and modifying the estimated depth at which the unloading effects occur.

The analog experiments, which used air-filled cracks in gelatin to simulate dike propagation (Anderson, 1905; Nakamura, 1977), simplify natural conditions. For example, they do not account for pre-existing structurally controlled anisotropies (e.g., faults, foliations, and fractures) or heterogeneous layering, both of which can influence dike trajectories in nature (Brune et al., 2023). The use of homogeneous gelatin leads to much simpler crack trajectories compared to models incorporating mechanical layering, such as rigidity (e.g., Urbani et al., 2018; Mantiloni et al., 2021) or density contrasts (Kavanagh et al., 2006). In addition, the experiments do not aim to reproduce the full geological complexities or simulate the supply of magma under natural conditions. Rather, they are explicitly designed and carefully scaled to isolate the primary stress-related mechanisms, particularly the interaction between tectonic and unloading stresses, regarding magma transport at the rift scale (Rivalta et al., 2019). Pre-existing fractures and faults can locally influence magma ascent, but their control on magma pathways may vary in different natural settings (Haug and Strecker, 1995; Robertson et al., 2016). Analog (Le Corvec et al., 2013) and numerical (Maccaferri et al., 2015) studies suggest that these structures exert a stronger control when they coincide with major topographic or structural features, such as fault scarps, but their influence diminishes in areas with relatively flat topography. Additionally, the finite size of the chosen setup may introduce boundary effects that influence dike paths (Corbi et al., 2016; Urbani et al., 2018).

Despite their limitations, the presented experiments reproduce key features observed in natural rift settings, and may explain the formation of volcanoes between rift segments, or rift flanks. These results are consistent with field observations (Keir et al., 2015; Muirhead et al., 2015), as well as analog (Corti et al., 2003; Mantiloni et al., 2021; Rahimi et al., 2025) and numerical models (Maccaferri et al., 2014; Ferrante et al., 2024), supporting the broader applicability of our findings.

5.2. Minor extension and asymmetric rifting: the Rhenish Massif

In low-strain rifts with low crustal unloading, such as the Rhenish Massif, volcanic centers tend to be widely distributed and predominantly monogenic. Analog experiments simulating unloading without applying any tensional stresses (Setup 5, Fig. 6b5) demonstrate that air-filled crack trajectories propagate laterally over longer distances with arcuate dips, often surfacing far from their injection points. Conversely, in a tensional stress field (Setup 4, Fig. 6b4), crack trajectories become more aligned and focused, narrowing the spatial distribution of the vents. These experimental observations may explain why, in an extremely low-strain region such as the Lower Rhine Rift, volcanism is highly scattered and dominated by monogenic vents.

Volcanic centers in the Rhenish Massif (Fry plots, inset in Fig. 2c) are organized along a N-S orientation (Tertiary) and NW-SE-oriented (Quaternary) main trends at the southeastern termination of the Lower Rhine Rift segment (Fig. 2c). In the experiments with tension (Setup 3 and 4; Fig. 6b3, b4) and in the presence of an analog wedge-shaped graben (Setup 3, 4 and 5; Fig. 6b3, b4, b5), stresses related to unloading progressively decrease toward the termination of the graben, facilitating magma ascent in these areas. This interpretation is supported by the DEM observations, which show that volcanic centers developed where a bounding fault loses throw at the rift segment termination (i.e., Siebengebirge and parts of the Hocheifel; Fig. 2c). While the low extension rates (0.07 mm/yr; Camelbeeck et al., 2020) are insufficient to exert a first-order control on magma pathways, the low-magnitude unloading (Fig. 3c) produced by the Lower Rhine Graben is still capable of influencing magma ascent. As a result, magma may either remain confined in the crust in the form of lens-shaped sills, as suggested for the Eifel (Eickhoff et al., 2024), or lead to scattered monogenic centers, such as those in the Rhenish Massif region.

5.3. Moderate extension and pronounced asymmetric rifting: Western Branch of the East African Rift System

The Western Branch of the East African Rift System exhibits a hybrid volcanic pattern, comprising large, polygenic volcanoes (i.e., Nyamuragira and Nyiragongo) and monogenic centers (i.e., Katwe), located either at the termination or on the eastern flank (i.e., Toro-Ankole and Virunga volcanic provinces) of the Albert, Edward, and Kivu rifts (Fig. 2d).

The distribution of volcanic centers at rift-segment terminations has often been attributed to fault-controlled magma pathways along transfer faults connecting adjacent rift segments (Ebinger et al., 1989). For instance, Corti et al. (2003) showed that during early continental rifting, tectonically-induced necking of the upper crust between offset rift segments creates lateral pressure gradients that force magma migration toward transfer faults. However, the distribution of historical eruption locations suggests that tectonic structures alone may not fully explain magma migration, pointing to additional stress-related mechanisms.

Analog experiments simulating the interaction between asymmetrical unloading and extension (Setup 3 and 4, Fig. 6b3, b4), together with DEM analysis, reveal two unloading-driven mechanisms that control magma transport in moderately extending, asymmetric rift settings. First, across-rift unloading has been demonstrated to influence magma trajectories in symmetric rift settings, where unloading promotes dike deflection and off-axis volcanism (e.g., Maccaferri et al., 2014; Ferrante et al., 2024). However, the results presented in this study highlight a distinct mechanism involving asymmetric unloading, which generates lateral stress gradients that deflect magma horizontally, away from the rift axis and toward the gentler margin of the graben. In the experiments simulating asymmetric rift geometry and extension (Setups 3 and 4; Fig. 6b3, b4), the air-filled cracks systematically deflected toward the shallower side of the mold that corresponds to the gentler rift margin. This pattern reflects the observed distribution of volcanic centers in the Toro-Ankole and Virunga regions, where arc-shaped vent alignments follow the eastern rift margin, opposite the deepest part of the basin identified in the DEM analysis (Fig. 3a). A clear example is Katunga volcano, located on the eastern flank of the Edward Rift, far from the rift axis and opposite the area of maximum subsidence (Fig. 3a). Although active tectonics in this region is characterized by ESE-WNW-trending extension (Ebinger et al., 1991), the spatial relationship between vent location and topographic asymmetry suggests that lateral unloading gradients can exert a first-order control on magma ascent in an asymmetric rift. Furthermore, in the case of along-rift unloading magma trajectories may propagate longitudinally beneath the graben. In all of the experiments, especially those without applied tension (Setup 5; Fig. 6b5, c5), air-filled cracks propagated beneath the mold and reached the surface at its termination. This behavior corresponds to the clustering of volcanism between adjacent rift segments, such as the Nyiragongo and Nyamuragira volcanoes, between the Edward and Kivu rifts. As grabens deepen toward their centers and become shallower near their terminations, the volume of removed material, and thus the magnitude of the unloading stress, diminishes along strike. This along-strike gradient creates favorable stress conditions for magma to erupt at the segment terminations.

These two unloading mechanisms are not mutually exclusive as they depend on basin geometry and the relative magnitudes of tectonic and unloading stresses. As discussed in Section 3.3, the ratio of these two stresses determines which mechanism eventually prevails. For example, when the ratio is low, unloading dominates; when the ratio is high, tectonic extension becomes the primary control. In this context, the Western Branch of the East African Rift System, with moderate extension rates (1–5 mm/yr; Saria et al., 2014) and pronounced asymmetric subsidence (Ebinger et al., 1991), is a remarkable example where both across- and along-rift unloading shape the spatial distribution of volcanism.

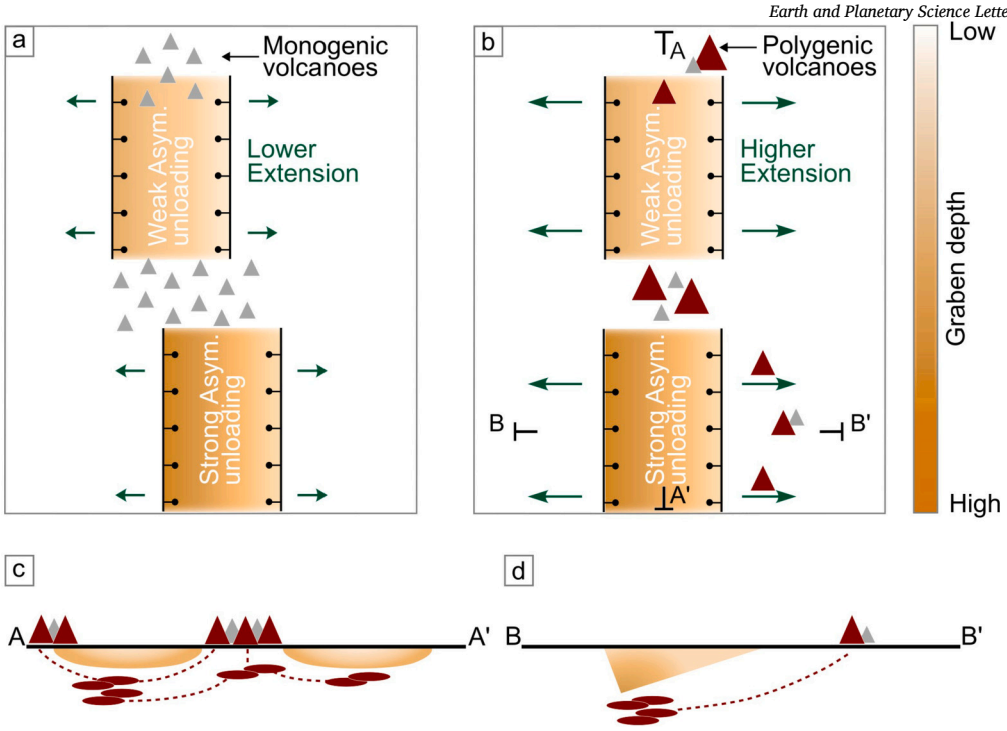

Fig. 8. Schematic across- and along-volcano distribution in rifts as a function of asymmetric unloading. a) Scenario with lower extension rate: in the upper graben, lower extension and weaker unloading result in scattered monogenic volcanic centers at the graben terminations. In the lower graben, the combination of lower extension and stronger unloading inhibits volcanism; b) Scenario with higher extension rate: in the upper graben greater extension with weaker unloading focuses polygenic (dark red triangles) and monogenic (gray triangles) volcanism at the graben terminations or within the graben. In the lower graben, higher extension with stronger asymmetric unloading redirects volcanism toward the gentler rift flank; c) Cross section parallel to the rift: magma sources (dark red ellipses) beneath the rift feed dikes (dark red dashed lines) that are deflected along the rift strike and erupt at the graben terminations. d) Cross section perpendicular to the rift: magmatic dikes are deflected across the rift, following a smoother topographic gradient and reaching the surface on the flank opposite the principal fault and rift depocenter.

5.4. High extension and moderate asymmetric rifting: Adda'do Magmatic Segment

The Adda'do Magmatic Segment displays a well-defined axial alignment of polygenic volcanoes at the graben terminations, but it lacks volcanism within and on the flanks of the grabens (Keir et al., 2006; Corti, 2009; Varet, 2017; Rees et al., 2023).

In the analog experiments with a tensional stress field (Setup 2; Fig. 6b2), as well as those experiments incorporating both unloading and tensional stresses (Setups 3 and 4; Fig. 6b3, b4), air-filled cracks predominantly aligned in an en-échelon pattern along the axis of the experimental box and at the termination of the mold depression. This pattern in the model matches the DEM observations, where the Gabillema, Yangudi, and Abida stratovolcanoes (Fig. 2e) are aligned along a NNE-SSW-oriented axis at the termination of the grabens. This observation raises an important question as to why volcanism is restrained within and across the rift in the high-strain Adda'do Magmatic Segment (about 5 mm/yr, Saria et al., 2014) when compared to the other two studied areas, and why magma does not erupt more readily in these locations.

The analog results suggest that while unloading beneath a rift occurs in all directions (both along and across the rift), tension predominantly acts in one direction and is oriented perpendicular to the rift axis. We suggest that by steering dikes towards the surface, stretching subdues unloading effects in the rift-perpendicular direction, restraining magma ascent towards the graben flanks. As there is no evidence of rift-parallel stretching, rift-parallel unloading remains unaffected. As a result of the combined effects of extension by normal faulting within the rift segments and along-strike unloading, magma propagation may be focused toward the rift termination rather than within the rift segment. Consequently, magmatic activity between adjacent rift segments plays a crucial role in accommodating an extension deficit through diking. Unless extension rates increase sufficiently to overcome extension accomplished by diking, repeated diking events may also inhibit the along-strike propagation of normal faults delimiting a graben. A likely example is the Yangudi volcano, which predates the onset of rifting and bisects the Adda'do Graben (Varet, 2017), suggesting that volcanic features can significantly influence the spatial evolution of rift segments. Ultimately, graben formation and dike-induced volcanism act as complementary processes in accommodating extensional strain. Similar patterns have been observed in volcanic arcs undergoing extension (Seebeck and Nicol, 2009) and extensional provinces subjected to high heat flow and volcanism, such as the Snake River Plain of Idaho, where Basin-and-Range normal faulting is substituted by diking in the area of the Yellowstone hotspot trail (Kuntz et al., 1992).

5.5. A conceptual framework for volcanism between adjacent rift segments

By comparing DEM-derived graben geometries with analog experiments under varying stress conditions, we propose a conceptual model in which the distribution of volcanic centers in rifts is governed by the close interplay between tectonic extension and crustal unloading. The relative dominance of these processes depends on rift maturity, extension rates, and graben asymmetry.

In low-strain rifts with weak asymmetric unloading (e.g., Rhenish Massif), neither tensional nor unloading stresses dominate magma pathways, thus promoting the formation of scattered monogenic centers between rift segments (Fig. 8a). In moderate-strain rifts with pronounced asymmetric unloading (e.g., Virunga), volcanism localizes both at rift-segment terminations and rift flanks (Fig. 8b, d). The more pronounced the graben asymmetry, the more developed the across-rift magma deflection. Finally, in high-strain rifts with moderate asymmetric unloading (e.g., Adda'do), volcanism localizes exclusively at the rift-segment terminations (Fig. 8b).

The mechanical interplay also triggers a cascading effect, where repeated dike intrusions can lead to sustained magma accumulation, the construction of volcanic edifices, and the formation of crustal magma reservoirs between rift segments. Over time, this process may generate stable, long-lived magma chambers capable of supporting persistent volcanic activity, as observed at Nyamuragira and Nyiragongo. This interpretation is consistent with observations by Pouclet et al. (2016), who describe a vertically and laterally connected magmatic system beneath both volcanoes.

In addition, the spatial correlation between volcanic centers and rift geometry, including their clustering at segment terminations or asymmetric deflection toward one flank of the rift, supports the interpretation that the distribution of volcanic edifices is also controlled by topography.

6. Conclusion

By combining DEM analysis with analog experiments that simulate magma ascent in the crust, we present a conceptual framework that demonstrates how along-axis unloading and rift-segment asymmetry control magma pathways in rifts. This approach provides a novel explanation for the concentration of volcanic centers at rift segment terminations and on the gently inclined margins of asymmetric rifts opposite border faults. It also explains the variability in the spatial distribution of volcanism observed across rifts with different extension rates and geometries. In addition to deep-seated, thermally driven processes forcing volcanism in these environments, the presented findings underscore the importance of incorporating unloading effects in combination with tectonic processes in models explaining the spatio-temporal characteristics of volcanism. These insights have thus direct implications for understanding magma transport, volcanic hazard, and geothermal resources in extensional provinces worldwide.

CRediT authorship contribution statement

Valentina Armeni: Writing – review & editing, Writing – original draft, Visualization, Methodology, Investigation, Funding acquisition, Formal analysis, Data curation, Conceptualization. **Lorenzo Mantiloni:** Writing – review & editing, Validation, Methodology, Formal analysis, Data curation, Conceptualization. **Bodo Bookhagen:** Writing – review & editing, Validation, Supervision, Software, Resources, Project administration, Methodology, Funding acquisition, Formal analysis. **Eleonora Rivalta:** Writing – review & editing, Validation, Supervision, Resources, Methodology, Investigation, Funding acquisition, Formal analysis, Conceptualization. **Valerio Acocella:** Writing – review & editing, Validation, Supervision, Methodology, Formal analysis, Conceptualization. **Manfred R. Strecker:** Writing – review & editing, Validation, Supervision, Resources, Project administration, Funding acquisition, Conceptualization.

Declaration of competing interest

The authors declare that they have no known competing financial interests or personal relationships that could have appeared to influence the work reported in this paper.

Acknowledgements

We thank the editor Lithgow-Bertelloni and two anonymous reviewers who contributed to improving the manuscript. This research was funded by Deutsche Forschungsgemeinschaft (DFG) grant BO 2933/6-1 (BB and VA), the University of Potsdam and KenGen Geothermal Power, Kenya (MS and VA), and the GFZ German Research Centre for Geosciences (ER and VA). LM was funded by DFG Grant N. RI 2782/6-1-ZO 277/3-1 and NERC grant NE/X013944/1. Analog experiments were conducted at the Bubble & Volcano Lab at GFZ. We also thank T. Dahm for discussion and S. Köster, S. Mikulla, R. Bauz, S. Mielitz, and P. Neuendorf for their assistance in the lab.

Appendix A. Supplementary material

Supplementary material related to this article can be found online at https://doi.org/10.1016/j.epsl.2025.119623.

Data availability

Data will be made available on request.

References

Acocella, V., 2021. Volcano-Tectonic Processes. Advances in Volcanology, vol. 567. Springer International Publishing, Cham.

Acocella, V., Ripepe, M., Rivalta, E., Peltier, A., Galetto, F., Joseph, E., 2024. Towards scientific forecasting of magmatic eruptions. Nat. Rev., Earth Environ. 5 (1), 5–22.

Amatulli, G., McInerney, D., Sethi, T., Strobl, P., Domisch, S., 2020. Geomorpho90m, empirical evaluation and accuracy assessment of global high-resolution geomorphometric layers. Sci. Data 7, 162.

Anderson, E., 1905. The dynamics of faulting. Trans. Edinb. Geol. Soc. 8, 387–402. https://doi.org/10.1144/transed.8.3.387.

Anderson, E.M., 1937. IX.—The Dynamics of the Formation of Cone-Sheets, Ring-Dykes, and Caldron-Subsidences. Proceedings of the Royal Society of Edinburgh, vol. 56. Royal Society of Edinburgh Scotland Foundation, pp. 128–157.

Bosworth, W., 1987. Off-axis volcanism in the Gregory rift, east Africa: implications for models of continental rifting. Geology 15, 397–400.

Boven, A., Pasteels, P., Punzalan, L.E., Yamba, T.K., Musisi, J.H., 1998. Quaternary per-potassic magmatism in Uganda (Toro-Ankole Volcanic Province): age assessment and significance for magmatic evolution along the East African Rift. J. Afr. Earth Sci. 26, 463–476.

Brune, S., Kolawole, F., Olive, J.A., Stamps, D.S., Buck, W.R., Buiter, S.J., Furman, T., Shillington, D.J., 2023. Geodynamics of continental rift initiation and evolution. Nat. Rev., Earth Environ. 4, 235–253.

Camelbeeck, T., Vanneste, K., Verbeeck, K., Garcia-Moreno, D., Van Noten, K., Lecocq, T., 2020. How well does known seismicity between the Lower Rhine Graben and southern North Sea reflect future earthquake activity?. In: Historical Earthquakes, Paleoseismology, Neotectonics and Seismic Hazard: New Insights and Suggested Procedures, pp. 53–72.

Corbi, F., Rivalta, E., Pinel, V., Maccaferri, F., Acocella, V., 2016. Understanding the link between circumferential dikes and eruptive fissures around calderas based on numerical and analog models. Geophys. Res. Lett. 43, 6212–6219. https://doi.org/10.1002/2016GL068721.

Corti, G., 2009. Continental rift evolution: from rift initiation to incipient break-up in the Main Ethiopian Rift, East Africa. Earth-Sci. Rev. 96, 1–53.

Corti, G., Bonini, M., Innocenti, F., Manetti, P., Mulugeta, G., Sokoutis, D., Cloetingh, S., 2003. Rift-parallel magma migration and localisation of magmatic activity in transfer zones. Acta Vulcanol. 14, 17.

Corti, G., Maestrelli, D., Bonini, M., Sani, F., 2025. Off-rift volcanism during continental rifting: observations and models with a focus on the Main Ethiopian Rift, East Africa. J. Afr. Earth Sci. 105590.

Ebinger, C.J., Casey, M., 2001. Continental breakup in magmatic provinces: an Ethiopian example. Geology 29, 527–530.

Ebinger, C.J., Deino, A.L., Drake, R.E., Tesha, A.L., 1989. Chronology of volcanism and rift basin propagation: Rungwe Volcanic Province, East Africa. J. Geophys. Res., Solid Earth 94, 15785–15803. https://doi.org/10.1029/JB094iB11p15785.

Ebinger, C.J., Karner, G.D., Weissel, J.K., 1991. Mechanical strength of extended continental lithosphere: constraints from the Western Rift System, East Africa. Tectonics 10, 1239–1256. https://doi.org/10.1029/91TC00579.

Eickhoff, D., Ritter, J.R.R., Hloušek, F., Buske, S., 2024. Seismic reflection imaging of fluid-filled sills in the west eifel volcanic field, Germany. Geophys. Res. Lett. 51, e2024GL111425. https://doi.org/10.1029/2024GL111425.

Fekiacova, Z., Mertz, D.F., Renne, P.R., 2007. Geodynamic setting of the tertiary hocheifel volcanism (Germany), Part I: 40Ar/39Ar geochronology. In: Ritter, J.R.R., Christensen, U.R. (Eds.), Mantle Plumes. Springer Berlin Heidelberg, Berlin, Heidelberg, pp. 185–206.

Ferrante, G., Rivalta, E., Maccaferri, F., 2024. Spatio–temporal evolution of rift volcanism controlled top–down by a deepening graben. Earth Planet. Sci. Lett. 629, 118593.

Forte, A.M., Whipple, K.X., 2019. The topographic analysis kit (TAK) for TopoToolbox. Earth Surf. Dyn. 7, 87–95.

Fossen, H., 2016. Structural Geology. Cambridge University Press.

Geluk, M.C., Duin, E.T., Dusar, M., Rijkers, R.H.B., Van den Berg, M.W., Van Rooijen, P., 1994. Stratigraphy and tectonics of the Roer Valley Graben. Geol. Mijnb., 129–141.

Global Volcanism Program, Smithsonian Institution, Venzke, E., 2024. Volcanoes of the World, (v. 4.3.4). Smithsonian Institution.

Grollimund, B., Zoback, M.D., 2001. Did deglaciation trigger intraplate seismicity in the New Madrid seismic zone? Geology 29, 175–178.

Gudmundsson, A., 1986. Mechanical aspects of postglacial volcanism and tectonics of the Reykjanes Peninsula, southwest Iceland. J. Geophys. Res., Solid Earth 91, 12711–12721. https://doi.org/10.1029/JB091iB12p12711.

Haug, G.H., Strecker, M.R., 1995. Volcano-tectonic evolution of the Chyulu Hills and implications for the regional stress field in Kenya. Geology 23, 165–168.

Hooper, A., Ófeigsson, B., Sigmundsson, F., Lund, B., Einarsson, P., Geirsson, H., Sturkell, E., 2011. Increased capture of magma in the crust promoted by ice-cap retreat in Iceland. Nat. Geosci. 4, 783–786.

Hubbert, M.K., 1937. Theory of scale models as applied to the study of geologic structures. Bull. Geol. Soc. Am. 48, 1459–1520.

Karner, G.D., Byamungu, B.R., Ebinger, C.J., Kampunzu, A.B., Mukasa, R.K., Nyakaana, J., Rubondo, E.N.T., Upcott, N.M., 2000. Distribution of crustal extension and regional basin architecture of the Albertine rift system, East Africa. Mar. Pet. Geol. 17, 1131–1150.

Kavanagh, J.L., Menand, T., Daniels, K.A., 2013. Gelatine as a crustal analogue: determining elastic properties for modelling magmatic intrusions. Tectonophysics 582, 101–111.

Kavanagh, J.L., Menand, T., Sparks, R.S.J., 2006. An experimental investigation of sill formation and propagation in layered elastic media. Earth Planet. Sci. Lett. 245, 799–813.

Keir, D., Bastow, I.D., Corti, G., Mazzarini, F., Rooney, T.O., 2015. The origin of along-rift variations in faulting and magmatism in the Ethiopian Rift. Tectonics 34, 464–477. https://doi.org/10.1002/2014TC003698.

Keir, D., Ebinger, C.J., Stuart, G.W., Daly, E., Ayele, A., 2006. Strain accommodation by magmatism and faulting as rifting proceeds to breakup: seismicity of the northern Ethiopian rift. J. Geophys. Res., Solid Earth 111, 2005JB003748. https://doi.org/10.1029/2005JB003748.

Kolb, M., Paulick, H., Kirchenbaur, M., Münker, C., 2012. Petrogenesis of mafic to felsic lavas from the Oligocene Siebengebirge volcanic field (Germany): implications for the origin of intracontinental volcanism in Central Europe. J. Petrol. 53, 2349–2379.

Konstantinou, K.I., 2024. Dike volume derived from seismicity as a gauge of fracture toughness and propagation dynamics. Sci. Rep. 14, 17593.

Kuntz, M.A., Covington, H.R., Schorr, L.J., 1992. Chapter 12: An Overview of Basaltic Volcanism of the Eastern Snake River Plain, Idaho. Geological Society of America.

Le Corvec, N., Menand, T., Lindsay, J., 2013. Interaction of ascending magma with pre-existing crustal fractures in monogenetic basaltic volcanism: an experimental approach. J. Geophys. Res., Solid Earth 118, 968–984. https://doi.org/10.1002/jgrb.50142.

Lippolt, H.J., 1983. Distribution of volcanic activity in space and time. In: Fuchs, K., Von Gehlen, K., Mälzer, H., Murawski, H., Semmel, A. (Eds.), Plateau Uplift. Springer Berlin Heidelberg, Berlin, Heidelberg, pp. 112–120.

Maccaferri, F., Acocella, V., Rivalta, E., 2015. How the differential load induced by normal fault scarps controls the distribution of monogenic volcanism. Geophys. Res. Lett. 42, 7507–7512. https://doi.org/10.1002/2015GL065638.

Maccaferri, F., Rivalta, E., Keir, D., Acocella, V., 2014. Off-rift volcanism in rift zones determined by crustal unloading. Nat. Geosci. 7, 297–300.

Maccaferri, F., Smittarello, D., Pinel, V., Cayol, V., 2019. On the propagation path of magma-filled dikes and hydrofractures: the competition between external stress, internal pressure, and crack length. Geochem. Geophys. Geosyst. 20, 2064–2081. https://doi.org/10.1029/2018GC007915.

Mantiloni, L., Davis, T., Gaete Rojas, A.B., Rivalta, E., 2021. Stress inversion in a gelatin box: testing eruptive vent location forecasts with analog models. Geophys. Res. Lett. 48, e2020GL090407. https://doi.org/10.1029/2020GL090407.

Merle, O., 2015. The scaling of experiments on volcanic systems. Front. Earth Sci. 3, 26.

Muirhead, J.D., Kattenhorn, S.A., Le Corvec, N., 2015. Varying styles of magmatic strain accommodation across the East African Rift. Geochem. Geophys. Geosyst. 16, 2775–2795. https://doi.org/10.1002/2015GC005918.

Nakamura, K., 1977. Volcanoes as possible indicators of tectonic stress orientation—principle and proposal. J. Volcanol. Geotherm. Res. 2, 1–16.

Namiki, A., Rivalta, E., Woith, H., Willey, T., Parolai, S., Walter, T.R., 2019. Volcanic activities triggered or inhibited by resonance of volcanic edifices to large earthquakes. Geology 47, 67–70.

Oliva, S.J., Ebinger, C.J., Rivalta, E., Williams, C.A., Wauthier, C., Currie, C.A., 2022. State of stress and stress rotations: quantifying the role of surface topography and subsurface density contrasts in magmatic rift zones (Eastern Rift, Africa). Earth Planet. Sci. Lett. 584, 117478.

Olive, J., Behn, M.D., Malatesta, L.C., 2014. Modes of extensional faulting controlled by surface processes. Geophys. Res. Lett. 41, 6725–6733. https://doi.org/10.1002/2014GL061507.

Pollard, D.D., Aydin, A., 1984. Propagation and linkage of oceanic ridge segments. J. Geophys. Res., Solid Earth 89, 10017–10028. https://doi.org/10.1029/JB089iB12p10017.

Pouclet, A., Bellon, H., Bram, K., 2016. The Cenozoic volcanism in the Kivu rift: assessment of the tectonic setting, geochemistry, and geochronology of the volcanic activity in the South-Kivu and Virunga regions. J. Afr. Earth Sci. 121, 219–246.

Purinton, B., Bookhagen, B., 2017. Validation of digital elevation models (dems) and comparison of geomorphic metrics on the southern Central Andean Plateau. Earth Surf. Dyn. 5, 211–237.

Rahimi, K., Bursik, M., Kavanagh, J.L., 2025. The influence of graben geometry on dike propagation. J. Volcanol. Geotherm. Res. 458, 108254.

Rees, R., Gernon, T.M., Keir, D., Taylor, R.N., Pagli, C., 2023. The spatial and volcanic evolution of Ayelu, Abida and Yangudi volcanoes in the Northern Main Ethiopian Rift–Southern Afar, Ethiopia. J. Volcanol. Geotherm. Res. 440, 107846.

Rees, W.G., 2000. The accuracy of digital elevation models interpolated to higher resolutions. Int. J. Remote Sens. 21, 7–20. https://doi.org/10.1080/014311600210957.

Rivalta, E., Corbi, F., Passarelli, L., Acocella, V., Davis, T., Di Vito, M.A., 2019. Stress inversions to forecast magma pathways and eruptive vent location. Sci. Adv. 5, eaau9784. https://doi.org/10.1126/sciadv.aau9784.

Rivalta, E., Taisne, B., Bunger, A.P., Katz, R.F., 2015. A review of mechanical models of dike propagation: schools of thought, results and future directions. Tectonophysics 638, 1–42.

Roberts, E.M., Stevens, N.J., O'Connor, P.M., Dirks, P., Gottfried, M.D., Clyde, W.C., Armstrong, R.A., Kemp, A.I.S., Hemming, S., 2012. Initiation of the western branch of the East African Rift coeval with the eastern branch. Nat. Geosci. 5, 289–294.

Robertson, E.A.M., Biggs, J., Cashman, K.V., Floyd, M.A., Vye-Brown, C., 2016. Influence of regional tectonics and pre-existing structures on the formation of elliptical calderas in the Kenyan Rift. Geol. Soc. (Lond.) Spec. Publ. 420, 43–67.

Rosendahl, B.R., 1987. Architecture of continental rifts with special reference to East Africa. Annu. Rev. Earth Planet. Sci. 15, 445–503.

Saria, E., Calais, E., Stamps, D.S., Delvaux, D., Hartnady, C.J.H., 2014. Present-day kinematics of the East African Rift. J. Geophys. Res., Solid Earth 119, 3584–3600. https://doi.org/10.1002/2013JB010901.

Schmincke, H.U., 2004. Volcanism, vol. 28. Springer Science & Business Media.

Schubert, S., Jung, S., Pfänder, J.A., Hauff, F., Garbe-Schönberg, D., 2015. Petrogenesis of Tertiary continental intra-plate lavas between Siebengebirge and Westerwald, Germany: constraints from trace element systematics and Nd, Sr and Pb isotopes. J. Volcanol. Geotherm. Res. 305, 84–99.

Schwanghart, W., Scherler, D., 2014. TopoToolbox 2–MATLAB-Based Software for Topographic Analysis and Modeling in Earth Surface Sciences. Earth Surface Dynamics, vol. 2. Copernicus Publications Göttingen, Germany, pp. 1–7.

Schäfer, A., Utescher, T., Klett, M., Valdivia-Manchego, M., 2005. The Cenozoic Lower Rhine Basin – rifting, sedimentation, and cyclic stratigraphy. Int. J. Earth Sci. 94, 621–639. https://doi.org/10.1007/s00531-005-0499-7.

Seebeck, H., Nicol, A., 2009. Dike intrusion and displacement accumulation at the intersection of the Okataina Volcanic Centre and Paeroa Fault zone, Taupo Rift, New Zealand. Tectonophysics 475, 575–585.

Upcott, N.M., Mukasa, R.K., Ebinger, C.J., Karner, G.D., 1996. Along-axis segmentation and isostasy in the Western rift, East Africa. J. Geophys. Res., Solid Earth 101, 3247–3268. https://doi.org/10.1029/95JB01480.

Urbani, S., Acocella, V., Rivalta, E., 2018. What drives the lateral versus vertical propagation of dikes? Insights from analogue models. J. Geophys. Res., Solid Earth 123, 3680–3697. https://doi.org/10.1029/2017JB015376.

Varet, J., 2017. Geology of Afar (East Africa). Springer.

Wang, B., Shi, W., Liu, E., 2015. Robust methods for assessing the accuracy of linear interpolated dem. Int. J. Appl. Earth Obs. Geoinf. 34, 198–206.

Watanabe, T., Masuyama, T., Nagaoka, K., Tahara, T., 2002. Analog experiments on magma-filled cracks competition between external stresses and internal pressure. Earth Planets Space 54, 1247–1261.

Watts, A.B., 2001. Isostasy and Flexure of the Lithosphere. Cambridge University Press.

Ziegler, P.A., 1992. European Cenozoic Rift System. Tectonophysics, vol. 208. Elsevier, pp. 91–111.